Geochemical consequences of melt transport in 2-D: The sensitivity of trace elements to mantle dynamics

Marc Spiegelman [*]

Lamont-Doherty Earth Observatory of Columbia University, Palisades, NY 10964, USA

Abstract

Dynamic models are presented to investigate the consequences of melting and melt transport for stable trace element geochemistry in open systems. These models show that including explicit melt transport in 2-D adds non-trivial behaviour because melts and residues can travel and mix along very different trajectories. Calculations are presented for both equilibrium and disequilibrium transport, and passive and active mid-ocean ridge flows. These calculations demonstrate that trace elements are sensitive to mantle dynamics and can readily distinguish between different end-member flow fields. Passive, plate-driven flow with strong melt focusing produces enrichments of incompatible elements. Active small-scale solid convection within the partially molten region, however, can lead to extreme dilution of incompatible elements, suggesting that this form of convection may not be significant beneath normal ridges. These calculations provide additional predictions about across-axis trends of geochemical variability and estimate the variation in concentrations that can occur even for a constant source. Many of these results are not seen in geochemical models that neglect melt transport and we discuss how this new behaviour affects the inferences drawn from simpler models.

Keywords: mantle; melts; transport; trace elements; geochemistry; open systems

1. Introduction

Trace elements have long been used to infer sources and degrees of melting of partially molten regions. Forward models used for interpreting these distributions range from single batch or fractional melting models [1,2] to more complicated models for integrated melting regions [3–12]. All of these models provide important constraints on the melting process; however, they do not include the fluid mechanics of melt transport. Because melt transport controls the sampling and mixing of melts from various parts of the melting region, it is unclear how including this process changes the inferences made from simpler models. Fortunately, with the advent of a more general theory of melting and melt migration [13–18] we can begin to quantify the observable effects of transport on geochemical signals.

Previous work considered the effects of melt transport on stable trace elements in 1-D but did not show behaviour that is significantly different from the classical solutions. In fact, for steady-state problems, the general equations reduce identically to the equations for batch and fractional melting, independent of melt transport [19] (see also [20]). For time-dependent problems, chromatographic separation of chemical fronts has been demonstrated [21,22], but

---

[*] E-mail: mspieg@ldeo.columbia.edu

these effects are transient and are sensitive to initial conditions. While previous results might suggest that transport does not have significant observable effects, many of these results stem from the very restrictive requirements imposed by 1-D steady-state systems and non-radiogenic elements. Ribe [23] presented an analytic solution for transport in an axisymmetric plume and showed that higher dimensional flows can produce results that differ substantially from the 1-D solutions. Spiegelman and Elliott [20] presented 1-D, steady-state transport models for short-lived uranium-series nuclides that showed that melt transport can have significant effects for elements that are sensitive to differences in transport time.

This paper continues to explore the geochemical consequences of melt transport by examining the behaviour of stable trace elements in a range of 2-D flows. These problems demonstrate that trace elements can be surprisingly sensitive indicators of the fluid mechanics of both melt and solid in the upper mantle. The first part of this paper develops the general equations for stable trace element transport in multiple dimensions for both equilibrium and disequilibrium melt transport. We then illustrate these equations by comparing the behaviour of trace elements in end-member 'passive' and 'active' flow regimes proposed for mid-ocean ridges. This comparison quantifies the sensitivity of geochemical signals to the underlying geodynamics and shows that geochemical signals can easily distinguish between the end-member flow fields. Finally, we discuss the behaviour of previous non-transport models in light of these new results and show how including melt transport can change the inferences made from simpler models.

2. Mechanics of melt transport

To calculate the behaviour of trace elements, we first must calculate the overall flow of solid and melt in a region of partial melting. The general equations for flow in deformable, permeable media were derived independently by several authors [13–15] and have been discussed in detail elsewhere [16–18,24,25]. The dimensional equations can be written:

$$\frac{\partial}{\partial t}\left(\rho_f \phi\right) + \nabla \cdot \left(\rho_f \phi \mathbf{v}\right) = \Gamma \tag{1}$$

$$\frac{\partial}{\partial t}\left[\rho_s(1-\phi)\right] + \nabla \cdot \left[\rho_s(1-\phi)\mathbf{V}\right] = -\Gamma \tag{2}$$

$$\phi(\mathbf{v}-\mathbf{V}) = \frac{-k_\phi}{\mu}\left[\nabla P - \rho_f \mathbf{g}\right] \tag{3}$$

$$\frac{\partial P}{\partial x_i} = \frac{\partial}{\partial x_j}\eta\left(\frac{\partial V_i}{\partial x_j} + \frac{\partial V_j}{\partial x_i}\right)$$
$$+ \frac{\partial}{\partial x_i}\left(\zeta - \frac{2}{3}\eta\right)\nabla \cdot \mathbf{V} + \bar{\rho}g\delta_{i3} \tag{4}$$

$$k_\phi \sim \frac{a^2 \phi^n}{b} \tag{5}$$

where ρ_f is the density of the melt; ϕ is the volume fraction occupied by the melt (i.e. porosity); $\mathbf{v}$ is the melt velocity; Γ is the rate of mass transfer from solid to melt (melting rate); ρ_s is the density of the solid matrix; $\mathbf{V}$ is the matrix velocity; k_ϕ is the permeability; μ is the melt viscosity and P is the fluid pressure and g is the acceleration due to gravity (which points downwards). η and ζ are the matrix shear and bulk viscosities and $\bar{\rho} = \rho_s(1-\phi) + \rho_f\phi$.

Eq. (1) and (2) conserve mass for the melt and solid matrix individually but allow mass transfer between solid and liquid via the melting rate Γ. Eq. (3) is a modified form of Darcy's law which governs the separation of melt from the matrix. Eq. (4) governs creeping matrix flow and shows that the pressure gradients that drive melt migration depend on the viscous deformation of the matrix, as well as the buoyancy difference between melt and solid. Eq. (5) gives the permeability as a function of the pore or channel spacing a, porosity and a dimensionless coefficient, b.

Eq. (5) is a convenient parameterization for a range of porosity/permeability relationships valid for small porosities ($\sim < 10$–20%). Because these equations are macroscopic, however, they do not make any a priori assumptions about the microscopic distribution of melt and solid. As long as Darcy's law governs the separation of melt and solid, these

equations are equally valid for flow in a grain-scale porous network, or in a network of veins or 'channels.' Variations in the microscopic distribution of melt and solid can change the functional form of the permeability but should not affect the qualitative fluid mechanics of melt migration. These microscopic variations, however, can have important effects on the ability of the melt to remain in equilibrium with the solid residue [26]. Section 3.1 and Section 3.2 demonstrate how different equilibration models can be consistently added to the basic fluid mechanics.

2.1. A useful example: passive and active ridge flows

To close Eqs. (1)–(5) for mantle melting systems requires a functional relationship for the mass-transfer rate Γ. In general, the melting rate depends on temperature, pressure and major element bulk com-
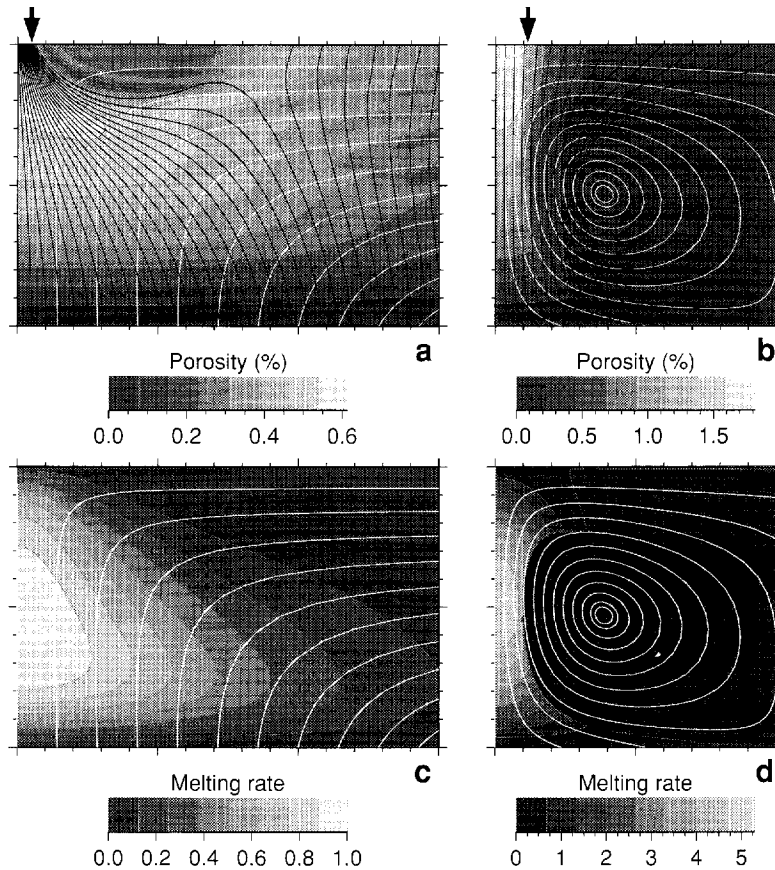

Fig. 1. 2-D solutions for the flow of melt and solid beneath mid-ocean ridges demonstrating the effects of passive vs. active mantle flow. Figures are vertical cross-sections of the right half of the melting region. The top two figures show porosity, melt flow (black curves) and solid flow (white curves). The bottom two figures show the dimensionless melting rate, which is proportional to upwelling rate for 'fertile' upwelling mantle. $\Gamma = 0$ for downwelling regions and previously depleted mantle. The vertical scale is the depth to where melting begins and there is no vertical exaggeration. All calculations use constant viscosity, a permeability exponent $n = 2$, and a nearly constant melting function $dF_o/dz = (0.25/d)\mathrm{erf}[z/(0.075d)]$. The erf taper at the bottom is used to minimize the generation of time-dependent solitary waves. (a) Plate driven flow (193 × 129 grid points). When shear is dominated by plate motion, the forced shear of the viscous matrix can produce large pressure gradients that focus the flow of melt. (b) Buoyancy driven flow (257 × 257 grid points). For lower viscosities or plate velocities, variations in melt content can drive additional small scale convection which narrows the width of the upwelling region. (c) Melting rate field for plate driven shear and (d) for buoyancy driven shear. The arrows in (a) and (b) indicate the width of the region where melts are sampled in Fig. 4 and Fig. 5.

position and requires additional conservation equations for energy, composition and equations of state. For mid-ocean ridges, however, a major simplification can be made by assuming that all melting is due to adiabatic decompression. In this case, the melting rate is proportional to the mantle upwelling rate and can be written:

$$\Gamma = \rho_s W \frac{dF_0}{dz} \qquad (6)$$

where W is the vertical component of the matrix velocity and dF_0/dz is the imposed change in the degree of melting with height in the melting region. Eq. (6) applies to upwelling mantle whose degree of depletion is $\leq F_0(z)$. There is no melting ($\Gamma = 0$) for downwelling regions or for mantle material that has been previously melted more than $F_0(z)$ (see Appendix A for calculating the local degree of depletion). For Fig. 1 we assume that the increase in the degree of melting is roughly linear with height.

Fig. 1 shows melt and solid flow fields, together with the porosity and melt production rate for end-member 'passive' and 'active' upwellings beneath mid-ocean ridges. Both calculations are consistent solutions of the full time-dependent equations and are similar to those discussed in [18] (with different parameters). Fig. 1 shows the results of long calculations that relax to steady state, due to the free-flux upper boundary condition and lack of sharp edges in the melting rate field. Important parameters for these runs are listed in Table 1 and the figure caption. Additional information on numerical methods is available upon request.

The principal difference between Fig. 1a and b is the relative strength of the two sources of mantle shear: plate driven flow and internal melt driven buoyancy. The ratio of these two stresses is expressed by the dimensionless parameter $R = (\phi_0 \Delta\rho g d^2)/(\eta U_0)$, which plays the same role that the Rayleigh number does in thermal convection. For small values of R, viscous shear is driven by the boundary conditions and resembles corner flow. Mantle upwelling and melting occur over a wide region, but the viscous stresses produced by plate driven corner flow cause melt to be focused towards the ridge axis [27–29]. The length scale of enhanced melt extraction is approximately $L \sim d/\sqrt{R}$. Thus, as R increases (e.g., lower viscosity or spreading rate), the width of the melt suction effect decreases; however, internal buoyancy forces become important and an additional small-scale convection roll is superposed on the corner flow [25,30–36]. In this case, solid mantle upwelling is focused into a narrow zone near the axis, producing much higher rates of melting.

Both solutions produce appropriate crustal thicknesses within a narrow neo-volcanic zone and have similar maximum and mean degrees of melting (Table 1). To distinguish between these flows using geophysical techniques requires being able to distinguish between approximately 0.5% and 2% partial melt with sufficient resolution to identify regions of no melt. While joint seismic and electro-magnetic methods may have sufficient discriminating power, we show here that these two flow fields produce remarkably distinct geochemical signatures.

Table 1
Some diagnostic features of the calculations in Fig. 1

variable	meaning	passive flow	active flow
R	buoyancy number	0.026	169
W_{max}/U_0	maximum upwelling velocity on axis relative to spreading rate	.637	3.26
w_0/U_0	reference melt separation velocity relative to spreading rate	18	18
F_{max}	maximum degree of melting on axis	20%	21%
F_B	bulk degree of melting for entire box	13%	17%
h/d	total crustal thickness relative to box depth	.08	.076

3. Equations of trace element transport

To add trace element transport to these flow fields requires specifying how melts interact with the solids that they pass through. Here we consider just the end-member models of equilibrium and disequilibrium transport. In equilibrium transport, the melt and solid remain in chemical equilibrium at all times. For disequilibrium transport, an instantaneous melt is produced that is locally in equilibrium with the solid source but the solid does not interact with any of the melt that passes through it. For 1-D steady-state systems, or systems where the melt does not separate from its source, equilibrium transport is equivalent to batch melting while disequilibrium transport is equivalent to perfect fractional melting for the solid and accumulated fractional melting for the melt [19,20]. Both equilibration models still assume that instantaneous melts are in equilibrium with the source. All other 'equilibrium melting' models must produce results that are intermediate between these two end-members. For extensions to disequilibrium melting models see [37,38].

3.1. Equilibrium trace element transport

In two-phase problems it is necessary to track the composition of both the melt and the solid. For equilibrium transport, however, the composition of the solid, c^s, is directly related to the melt composition, c^f, by the bulk partition coefficient, D; that is, $c^s = Dc^f$. Thus, it is sufficient to conserve the bulk mass of any element with:

$$\frac{\partial}{\partial t}\left[\rho_f\phi + \rho_s(1 - \phi)D\right]c^f$$
$$+ \nabla\cdot\left[\rho_f\phi\mathbf{v} + \rho_s(1 - \phi)\mathbf{V}D\right]c^f = 0 \qquad (7)$$

which states that the change with time in total mass of the element per unit volume depends only on the net flux of mass in the melt and solid. Additional source terms can also be added for diffusion and radioactive decay/production [20]. Scaling arguments for diffusive length scales, however, show that diffusion only causes smoothing of trace element concentrations over length scales of the order of 1–10 m for the low chemical diffusivities and high melt velocities expected here.

Moreover, if we neglect chemical diffusion, Eq. (7) can be rewritten and solved in a more tractable form. Expanding and substituting Eq. (1) and (2) for conservation of mass of bulk melt and solid, Eq. (7) becomes:

$$\frac{\partial c^f}{\partial t} + v_{eff}\cdot\nabla c^f = c^f\left[\alpha\Gamma + \dot{D}\right] \qquad (8)$$

where:

$$\mathbf{v}_{eff} = \frac{\rho_f\phi\mathbf{v} + \rho_s(1 - \phi)D\mathbf{V}}{\rho_f\phi + \rho_s(1 - \phi)D} \qquad (9)$$

is the effective velocity of each tracer. $\mathbf{v}_{eff}$ is a weighted average of the melt and solid velocity fields. If a tracer is completely incompatible ($D = 0$) it travels with the melt and $\mathbf{v}_{eff} = \mathbf{v}$. Likewise, a completely compatible element ($D \rightarrow \infty$) travels along the solid flowlines. Intermediate compatibility elements travel on flowlines defined by $\mathbf{v}_{eff}$. The term:

$$\alpha = \frac{D - 1}{\rho_f\phi + \rho_s(1 - \phi)D} \qquad (10)$$

is a weighting factor which determines how melting changes the concentration of a tracer in the melt. If $D = 1$, melting has no effect. Melting causes dilution of incompatible elements and enrichment of compatible elements. Finally:

$$\dot{D} = \frac{\rho_s(1 - \phi)}{\rho_f\phi + \rho_s(1 - \phi)D}\left[\frac{\partial D}{\partial t} + \mathbf{V}\cdot\nabla D\right] \qquad (11)$$

is an additional source term that depends on changes in the bulk partition coefficient as measured in the frame of the solid. For systems where the partition coefficients vary only as a function of depth, the bracketed part of this term becomes $Wd D/d z$ (see Section 5 for an example).

Eq. (8) is a transport equation that states that individual trace elements travel along trajectories defined by $\mathbf{v}_{eff}$ and change their composition by the amount of melting and any changes in bulk partition coefficient experienced along the trajectory. In the simplest case, where the melt does not separate from the solid, the tracer trajectories are equal to solid trajectories and these equations reduce to those for batch melting in a frame fixed to the solid. In
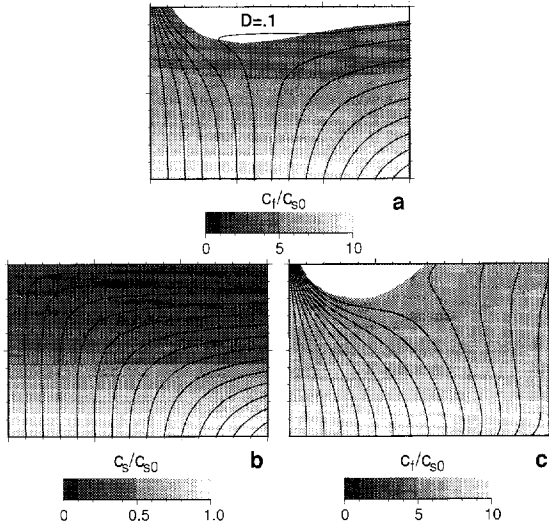
Fig. 2. Comparison of trace element trajectories and concentrations for a moderately incompatible element with bulk partition coefficient $D = 0.1$ in a passive flow geometry. (a) Equilibrium transport. Grey shades show melt concentration normalized to solid source c^f / c_o^s. Solid lines are selected trace element trajectories which are intermediate between the solid and melt flow field (compare to b and c). (b) Disequilibrium transport: solid flow field and concentration. (c) Disequilibrium transport: melt flow field and concentration. The melt concentration is the integral of all the instantaneous melts produced along the melt flow path weighted by the local melt flux. Instantaneous melt compositions are c^s / D. Melt concentrations are ill-defined in the white areas in (a) and (c) because they involve regions that are not completely sampled by melt trajectories that connect to the base of the melting zone.

general, however, melt and solid do not travel together and the local melt concentrations can vary significantly from batch melts. To calculate the tracer trajectories, it is useful to rewrite Eq. (8) as a system of ordinary differential equations which reduces the problem to a particle tracking problem (see Appendix A.1). For non-diffusive problems, these particle tracking techniques are much faster and much more accurate than standard finite-difference or finite-element schemes. Fig. 2a shows concentrations and trajectories for equilibrium transport of a moderately incompatible element with constant partition coefficient $D = 0.1$.

3.2. Disequilibrium trace element transport

In disequilibrium trace element transport, the melting of the solid phase is decoupled from the composition of the transported melts and we need to conserve melt and solid compositions separately using:

$$\frac{\partial}{\partial t}\left[\rho_s(1 - \phi)c^s \right] + \nabla \cdot \left[\rho_s(1 - \phi)\mathbf{V}c^s \right]$$

$$= -\Gamma \frac{c^s}{D} \qquad (12)$$

$$\frac{\partial}{\partial t}\left[\rho_f \phi c^f \right] + \nabla \cdot \left[\rho_f \phi \mathbf{v}c^f \right] = \Gamma \frac{c^s}{D} \qquad (13)$$

Eq. (12) governs conservation of composition for the solid phase and states that changes in solid composition depend on the flux of solid and a sink term that is the production rate of an instantaneous melt that is locally in equilibrium with the solid source (i.e. $c^f_{inst} = c^s / D$). These equations do not assume that D is constant. Eq. (13) is the corresponding conservation equation for the melt composition where the source term is the instantaneous melt produced by the solid. The sum of these equations must equal zero, because total mass is conserved.

These equations can also be combined with bulk conservation of mass to yield more numerically tractable forms. Expanding (12) and substituting Eq. (2) yields:

$$\frac{\partial c^s}{\partial t} + \mathbf{V} \cdot \nabla c^s = \left(\frac{1}{D} - 1 \right)c^s \frac{\Gamma}{\rho_s(1 - \phi)} \qquad (14)$$

Thus if $\mathbf{V}$, D, Γ and ϕ are known, the trace element concentration in the residual can be calculated and is very close to what would be calculated for a fractionally melted solid in the absence of melt separation. Given the concentration of the solid source, the melt composition is calculated by combining Eq. (13) and (1) to give:

$$\frac{\partial c^f}{\partial t} + \mathbf{v} \cdot \nabla c^f = \left(\frac{c^s}{D} - c^f \right)\frac{\Gamma}{\rho_f \phi} \qquad (15)$$

Appendix A.1 provides the necessary details for the solution of these equations as systems of ordinary differential equations. Fig. 2b,c shows solid and melt concentrations and trajectories for disequilibrium transport of a moderately incompatible tracer with $D = 0.1$.

4. Application to passive and active ridge flows

This section illustrates the behaviour of the equations of trace element transport in the two end-member flow regimes shown in Fig. 1. To emphasize the effects of melt transport processes, we consider the simplest case where each tracer has a constant bulk partition coefficient throughout the melting region and a homogeneous source at the initiation of melting. Once the fundamental behaviour is understood, the discussion shows how to extend these calculations to more complex/realistic systems.

4.1. Results

Fig. 3 shows trace element concentrations calculated for a wide range of partition coefficients. These are the concentrations of trace elements in the melts that exit the top of the model (as these are the only melts that could actually be observed). As a first comparison, Fig. 3b shows patterns for melts 'erupted' directly at the ridge axis ($x = 0$) for the four end-member transport models, as well as for a 1-D melting column with the same degree of melting as the ridge axis (here $F_{max} \sim 20\%$). Each curve shows the concentration of tracer in the melt normalized to the solid source (c^f/c_0^s). Because the sources are identical in all models, any variation between curves is due only to the fluid dynamics or the equilibration model.

For very incompatible elements ($D \sim < 0.001$) variation between equilibration models is negligible. However, differences in flow regime can cause up to a factor of 5 difference in concentration between passive and active flows. In particular, small-scale convection within the partially molten region causes strong depletions in incompatible elements and produces trace element patterns where the concentration of extremely incompatible elements relative to source is *less* than that of moderately incompatible ones. This behaviour is not found in standard geochemical models. Compared to the 1-D melting column, the axial melts for active flow are depleted in incompatible elements by over a factor of 2, while those for passive flow are enriched by a similar amount. Within any melting model, however, different equilibration models produce only a maximum $\sim 20\%$ difference in concentration for the moderately incompatible ele-
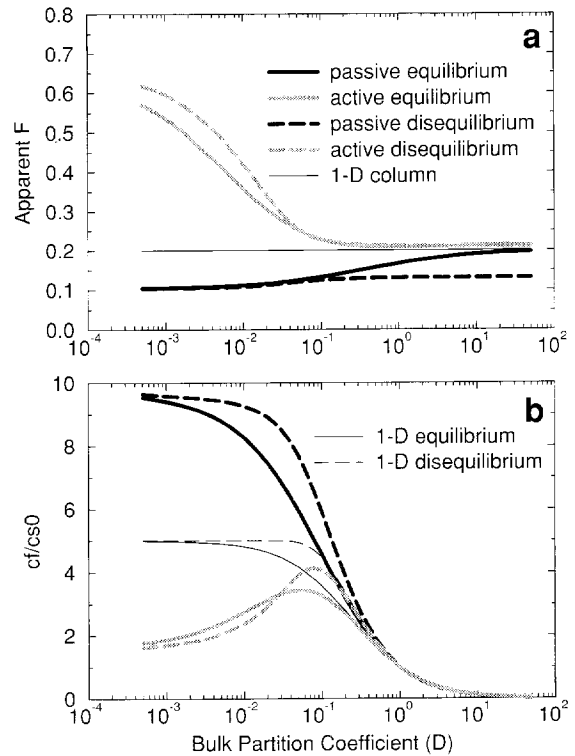

Fig. 3. Composition and apparent degrees of melting as a function of bulk partition coefficient for melts sampled directly on axis ($x = 0$) for passive and active flow models, using both equilibrium and disequilibrium transport. The bottom figure (b) shows concentration of trace elements in the melt relative to the source concentration in the solid. This figure also shows concentrations expected for a 1-D steady-state melting column with 20% melting and equilibrium and disequilibrium transport. 1-D equilibrium concentrations are identical to 20% batch melts; disequilibrium is identical to 20% accumulated fractional melts. The top figure (a) shows the 'apparent degree of melting' inferred from trace element patterns using the appropriate equilibration model. While the 1-D steady-state column has a constant $F_{app} = 0.20$ independent of D or equilibration model, the 2-D transport models show widely variable apparent degrees of melting.

ments that have partition coefficients comparable to the degree of melting ($0.02 \sim < D \sim < 0.2$). This result is typical of previously published geochemical models (e.g. [8,39]).

Another way to view the results of these calculations is in terms of the 'apparent degree of melting', F_{app}. F_{app} is defined as the degree of melting we would calculate from c^f/c_0^s given the bulk partition coefficient and an appropriate equilibration model.

The apparent degree of melting for equilibrium transport is calculated relative to a single batch melt using:

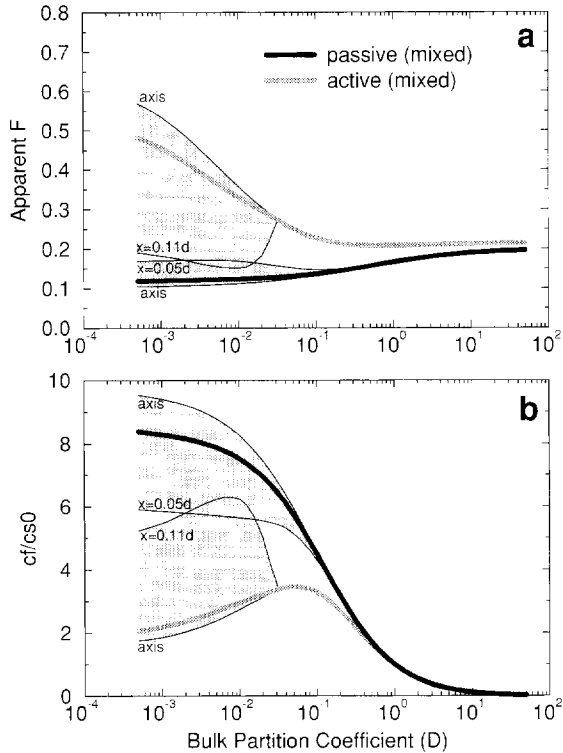$$F_{app} = \frac{1 - c'D}{c'(1 - D)} \tag{16}$$

Fig. 4. Across-axis variation in melt compositions and apparent degree of melting (a) and melt compositions (b) for passive and active flows: Equilibrium melting. The lower plot shows trace element concentrations in the melt normalized to the solid source. For each flow model, the thin black line marked axis is the trace element pattern for melts sampled at the axis ($x = 0$) and is identical to that shown in Fig. 3. The thin line marking the other bound of the shaded region is the trace element pattern for melts sampled at the points marked by arrows in Fig. 1 ($x = 0.05d$ for passive flow and $x = 0.11d$ for active flow; d is the depth of the box). By this point, both models have extracted ~ 80% of the total melt produced to form the crust. Melts sampled anywhere between the axis and the off-axis bound will have trace element patterns that lie in the grey shaded area. The thick black line shows the concentration of a melt produced by mixing all the individual melts in the grey region weighted by their relative fluxes (Eqs. (4 NO TRANSLATION 18)). Note that different trace elements can have large differences in the range of variation, up to about a factor of 2 for extremely incompatible elements, even though the sources are identical.
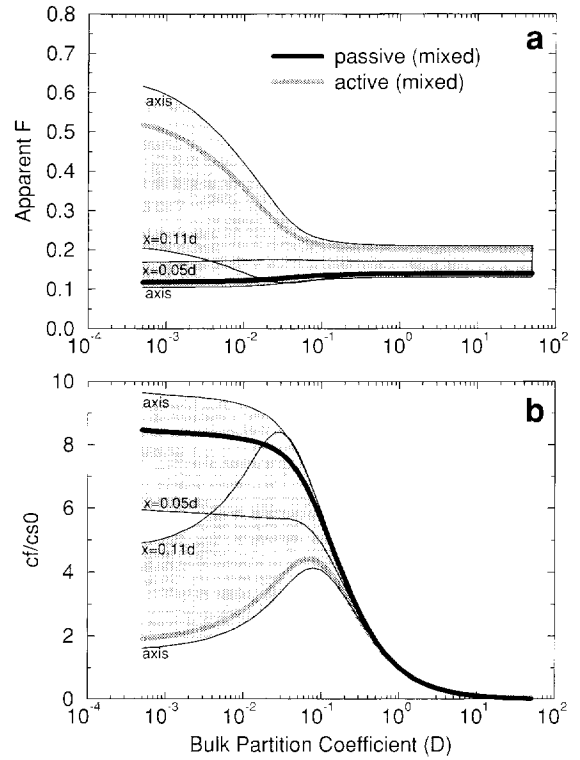

Fig. 5. Same as Fig. 4 but for disequilibrium transport. While the quantitative results change slightly, the qualitative trends remain the same as those of equilibrium transport. The biggest difference between the models is in F_{app} inferred for compatible elements, although the actual measurable differences in concentration for these elements are quite small.

where $c' = c^f/c_0^s$. Normalizing to a batch melt is appropriate because a 1-D steady-state column undergoing equilibrium transport produces melts that are identical in concentration to batch melting (Fig. 3b). The apparent degree of melting inferred using Eq. (16) for melts that leave the top of such a column would be $F_{app} = F_{max}$ for all partition coefficients (Fig. 3a). The apparent degree of melting for disequilibrium transport is defined using the equation for an accumulated fractional melt:

$$c' = \frac{1}{F_{app}}\left[1 - \left(1 - F_{app}\right)^{1/D}\right] \tag{17}$$

because a 1-D column undergoing disequilibrium transport produces melts that are identical to an accumulated fractional melt. Again, the melts at the top of such a column would record an apparent degree of melting of F_{max} for all elements.

In the 2-D models, however, the apparent degree of melting varies with partition coefficient and equilibration model, even directly on-axis. In general, axial melts for plate driven flow give apparent degrees of melting for all elements that are less than the maximum degree of melting. Buoyantly driven flows give melts that appear to have melted to degrees greater than F_{max}. The differences are most extreme for the highly incompatible elements. Plate driven flow returns $F_{app} \sim 10\%$, while strongly buoyantly driven flow produces ultra-depleted melts that appear to have been generated by melting the source by 50–60%. These depletions are sufficiently large to suggest that strongly melt driven buoyant flow within the partially molten region should be observable geochemically.

The large departures from 1-D melting models are a direct result of the 2-D effects of melt focusing by passive flow and solid focusing by active flow. Section 4.2 and Appendix A.2 explain how the models work in detail. To aid in the explanation, however, it is useful to understand the across-axis variation in melt compositions produced by these calculations. Fig. 5 show the range of melt concentrations produced by passive and active flows within the 'crustal accretion zone', whose width is indicated by arrows in Fig. 1. This is the region over which both models have extracted $\sim 80\%$ of the total melt production to form the crust. Fig. 4 shows results for equilibrium transport while Fig. 5 shows disequilibrium transport. For each flow regime, the total field of variability (grey shading) is bounded by the two trace element patterns for the axis ($x = 0$) and the off-axis edge of the accretion zone ($x = x_f$). Trace element patterns for intermediate points tend to vary smoothly (but not linearly) between the two bounding patterns. The heavy solid lines are the average trace element concentration patterns for the entire accretion zone calculated by pooling all the individual melts weighted by their relative fluxes, that is:

$$\bar{c}(D, x_f) = \frac{\int_0^{x_f} \phi w c'(D) \, \mathrm{d}x}{\int_0^{x_f} \phi w \, \mathrm{d}x} \qquad (18)$$

The mean melt concentrations are always closer to the axial concentrations because the melt flux is a maximum on-axis and decreases away from the axis in both solutions. Increasing the width of the accre-

tion zone to include 90% of crustal production increases the size of the variability fields (which unfortunately clutters the plots) and causes the mean concentrations to converge slightly. The mean concentrations remain distinct, however, and incompatible elements in the active flow calculation still record $F_{app} \sim 40\%$.

Figs. 4 and 5 show several important features. First, the overall variation in concentration for any tracer (i.e. the size of the grey area) is a function of the partition coefficient and can range from a factor of ~ 2–3 in extremely incompatible elements down to nothing for elements with $D > \sim F_{max}$. For a slightly larger accretion zone, the variation in incompatibles is ~ 4. If this variation was interpreted using non-transport models, it would most readily be attributed to source variations. However, the sources are identical in these forward calculations, and this variation is due to the fluid mechanics of mixing.

The most surprising result of these calculations is that the sense of depletion relative to what is recorded on-axis is different for active and passive flows. Small-scale convection within the melting zone causes the largest depletions to occur on-axis and melts become more enriched off-axis, with the farthest off-axis melts representing extremely enriched melts. Melt focusing due to passive flow, however, produces melts that are most enriched on-axis and becomes more depleted away from the axis (at least in the accretion zone; melts far away from the axis are still relatively enriched melts). This behaviour is not found in non-transport models and has important implications for estimates of the depth and width of melt extraction (see Section 4.3 and Section 5).

4.2. How it works

All of these results are a direct response of including melt transport in 2-D. Appendix A.2 shows mathematically that these results are an expected consequence of the governing equations; however, here we develop a more qualitative physical argument to explain this behaviour. The important point is that in 2-D (and 3-D) open systems, melt and solid do not travel together. While solid flow dictates the shape of the melting regime, it is the fluid mechanics of melt transport that control how that region is

sampled and how the local melts are mixed. In general, all melting models include two stages of melt mixing: the local mixing of melts along trace element trajectories and then the secondary mixing of melts from different trajectories (e.g. in a crustal magma chamber). In non-transport models, the first stage of mixing is implicitly assumed to occur along solid flow lines, which is why identical results are obtained for simple 'melting column models' and models that include the solid flow field (e.g. [4,6,12]). Melt transport models, however, allow trace element trajectories to cross solid flow lines and accumulate instantaneous melts produced from a wide range of solid residues. Thus, the local concentration of trace elements in the melt can vary significantly from those calculated in melting column models. Ad hoc mixing of melts and residues can still be done in non-transport models. However, without including the full fluid mechanics, it is almost impossible to guess consistently how melt concentrations will change.

Once the flow of melt is included, the results of these calculations are readily understood. Inspection of the melt and solid flow fields in Fig. 1b,d shows why convergent solid flow within the partially molten region leads to large depletions of incompatible tracers. Consider the region near the axis that is approximately $0.1d$ wide and contains the region of maximum melt production. The only source of incompatible elements for this region comes from an area at the base, which is approximately $0.15d$ wide, because trace element trajectories for highly incompatible tracers approximate the melt flow trajectories. The amount of solid that enters this region, however, comes from a much wider region (around $0.6d$ wide). The bulk of this solid, however, has already lost most of its highly incompatible elements to off-axis melt trajectories before it reaches the region of maximum melt production. Any further melting of this solid near the axis only contributes to the dilution of incompatible elements. More compatible elements do not show this depletion because they are less readily stripped from the solid by melting and are not released until they are within the maximum melting region.

The explanation for the enrichment in incompatible elements caused by melt focusing is similar but works in the opposite way. For the region near the

axis, only a small portion of the solid has melted; however, we have added to it a large flux of incompatible elements from off-axis. Melts become more depleted with distance from the axis, however, because tracer trajectories near the edge of the accretion zone sample the shallowest and most depleted residues.

It is important to note that the largest effects in either model occur directly on the ridge axis. While the axis might appear to be reasonably approximated by a 1-D problem, it is not. In 1-D there are severe constraints on both solid and melt flow velocities imposed by conservation of mass (see Appendix A.2). In 2- and 3-D these constraints are much weaker and locally melt or solid velocities can be quite different from the 1-D requirements. The fast upwelling of solid on the axis during small-scale convection is due to the 2-D convergence of solid flow. Likewise, the high fluxes of melt near the top of the passive flow calculation are due to the 2-D convergence of melt. It is these variations in melt and solid flux that lead to the departures from the 1-D solutions and allow for melts on-axis to have apparent degrees of melting that differ significantly from F_{max}. Appendix A.2 develops these arguments more rigorously.

4.3. Comparison to non-transport models

By including explicit melt transport, these calculations add new behaviour that is not seen in previous non-transport geochemical models, and this section emphasizes how this new behaviour affects the inferences drawn from simpler models. It should be stressed that the behaviour of non-transport models is still contained in these new calculations because all models fundamentally conserve mass. If *all* the melt that was produced in Fig. 1a,b were extracted and mixed together, then the mean concentrations of elements in the pooled melts must be independent of the pooling process. However, the transport models retain spatial information about local variations in melt concentrations whereas non-transport models tend to assume complete extraction and mixing to produce bulk averages.

The assumptions of complete extraction and pooling of melts have several consequences for the output of non-transport models. First, by producing bulk

averages, these models significantly reduce the expected variation in concentrations and apparent degree of melting. Even the more realistic melting models that allow mixing of melts from regions with variable degrees of melting (e.g. [4,6–8,10–12,39]) are still well approximated by a single batch or accumulated fractional melt with a nearly constant apparent degree of melting that is comparable to the bulk degree of melting F_B ([39] provides a useful summary). In particular, the non-transport models tend to produce a single average concentration for highly incompatible elements that is always greater than or equal to the concentrations of moderately incompatible elements. Thus, these models could not account for the unusual depletion signatures of active flow without invoking a previously depleted source. More generally, non-transport models do not produce scatter in highly incompatible elements and are, therefore, forced to ascribe any variation in these elements to source heterogeneity or 'mantle metasomatism'. While source heterogeneity is clearly demonstrated by isotopic heterogeneity and large variations in element abundances, it is worth noting that the fluid–dynamic models can produce a factor of ~ 2–4 variation in concentration of closely spaced melts with a homogeneous source. Thus, any observed scatter or local depletion could actually be a signal of the melt transport process.

The second consequence of complete extraction and pooling is that these assumptions lose information about spatial variability. More seriously, the non-transport models can be slightly misleading about expected spatial variability. In general, these models predict that the most depleted melts should occur on-axis (i.e., in a melting column with degree of melting F_{max}) with increasing enrichment occurring off-axis. These models have the most enriched melts in the distal 'wings' of the melting region. Thus, to produce melts with mean concentrations that are representative of F_B, the non-transport models are forced to assume efficient extraction of melt from nearly the entire melting region. When melt transport is included, however, the axial melts do not necessarily have an apparent degree of melting of F_{max} and the need for complete melt extraction changes. In the case of active flow, the problem is exacerbated because convergent solid flow within the partially molten region produces axial melts with apparent degrees of melting that are greater than F_{max}. In these models, the low-degree melts required to balance the excessive depletion on-axis occur as a small flux of extremely enriched melts that are far from the axis. Unless all of this material can make its way to the ridge, the mixed axial melts will still appear strongly depleted. In the case of passive flow, however, strongly convergent melt flow produces enriched axial melts with apparent degrees of melting that are already close to or less than F_B. Because adjacent off-axis melts are actually more depleted than the axial melts, it is possible in these problems to leave out regions of off-axis melts without producing a strong geochemical signature. If non-transport models are used to interpret these melts, however, incorrect inferences can be made about the depth and extent of melting. The discussion provides a concrete example. More generally, these transport models suggest that there may be important signals inherent in the spatial variability of erupted melts and encourage the collection of well located geochemical data.

Predictions about spatial variability and the ability to produce trace element signatures that cannot be explained using non-transport models provide the best tests of the transport calculations. Careful analysis of closely sampled data from the East Pacific Rise indicates that nearby off-axis melts appear to have slightly higher degrees of melting (J. Reynolds, pers. commun. [40]), suggesting that some mechanism for convergent melt flow is present beneath the EPR. Evidence for strong solid convection within the partially molten region appears to be less common, although some depletion mechanism may be needed to explain the trace element signatures at anomalous ridges such as Kolbeinsey (C. Langmuir, pers. commun.). A full explication of this data is beyond the scope of this paper and will be presented elsewhere.

5. Discussion

These 2-D transport models show that stable trace elements can be a sensitive indicator of mantle flow dynamics and can readily distinguish between different mantle flow fields. All of these results are natural consequences of the extra degrees of freedom afforded by 2-D flow fields. While the consequences of a wider range of flow regimes and 3-D flows need

to be explored, the solutions presented here demonstrate two basic effects that should carry over to more complex systems: flow fields where the melt flow is convergent relative to the solid flow should produce enrichments in incompatible elements while solid flow fields that converge within the zone of partial melting should generate dilution of incompatible elements. This result applies to any region of partial melting, including the deep regions of small-degree melting that have been suggested by several authors (e.g. [10,25]).

For the active flow calculation presented here, the extreme depletion of highly incompatible elements and the unusual trace element patterns produced by convergent solid flow, suggests that this flow field is probably inconsistent with MORB geochemistry, unless the MORB source is significantly more enriched in incompatible elements than is usually accepted (e.g. [41–43]). The depletion effect of this particular flow field, however, is probably a maximum because all the convergent flow occurs within the partially molten region. While this flow field is a reasonable approximation to calculations where melting induces large reductions in solid viscosity (e.g. [32]), previously published flow fields [31–35] also include additional processes and boundary conditions that modify the solid flow and will change the magnitude of the depletion effect. While I suspect that many of these flows will produce some degree of depletion, a full quantitative evaluation of these models remains to be done. The point of this paper is that it is essential to show that a model is both physically *and* geochemically consistent with observations because models with similar crustal thickness and mean degrees of melting can have radically different geochemical signatures.

The main purpose of this paper is to emphasize the geochemical consequences of fluid mechanics without the added complexity imposed by 'real' systems. Given a basic understanding of these processes, however, the next step is to extend the models to more general elements so that the model output can be compared with observations. While a comprehensive model is beyond the scope of this paper, here we present one final example that demonstrates how to extend the models, in this case, to include the behaviour of rare earth elements. These initial results provide a more geologically

Table 2
Phase proportions and bulk partition coefficients for 2-layer model

Phase Proportions					
field	Ol	Opx	Cpx	Garnet	Sp
Spinel	0.577	0.29	0.10	0.00	0.033
Garnet	0.569	0.22	0.066	0.1450	0.00

Bulk Partition coefficients					
field	La	Ce	Pr	Nd	Sm
Spinel	0.0065	0.0112	0.0171	0.0237	0.0298
Garnet	0.0057	0.0105	0.0192	0.0285	0.0515
	Eu	Gd	Tb	Dy	Ho
Spinel	0.0358	0.0356	0.0374	0.0404	0.0395
Garnet	0.0705	0.0962	0.1341	0.1811	0.2487
	Er	Tm	Yb	Lu	
Spinel	0.0396	0.0416	0.0432	0.0464	
Garnet	0.3170	0.4634	0.6140	0.8295	

relevant illustration of the consequences of melt transport and add insights into the behaviour of current rare earth inversions (e.g. [12]).

This model has two important extensions over the ones shown in Figs. 1–5. First, it allows for an arbitrary 'melting function', dF_0/dz, as this may vary with improved understanding of major element melting (e.g. [44–46]). Second, this model allows for a layered partition coefficient structure where each element can have up to two bulk partition coefficients depending on the depth. This feature is particularly important for the heavy rare earths (and the U-series nuclides) that are strongly affected by the presence of garnet. Table 2 gives the bulk partition coefficients used for the 14 rare earth elements in this calculation. Fig. 6 shows equilibrium transport trajectories for La and Lu and demonstrates how heavy and light rare earths can be sampled from different regions of the mantle and are affected differently by the presence of garnet. Fig. 7 shows the calculated REE concentrations for each of the nine trajectories that exit near the ridge axis, as well as the mean concentration of the mixture of all of these melts.

Figs. 6 and 7 show several features. First, even with depth-dependent partition coefficients, the overall behaviour is the same as shown previously for passive flow calculations; that is, the axial melts show the highest concentrations (and steepest

= 'deepest') REE patterns, whereas off-axis melts appear to show higher degrees of shallower melting. More interesting, however, is that the overall REE pattern shows a mild 'garnet signature', even though the shallowest melts for all trajectories are actually in equilibrium with a spinel peridotite. The reason for this behaviour is apparent from the relative behaviour of La and Lu trajectories shown in Fig. 6. Because Lu behaves more compatibly in the garnet field, it follows the solid flow field until it is liberated in the spinel field, resulting in a narrower region of extraction for Lu. La, however, is incompatible in both fields and is extracted from a wider region. This behaviour is true, to a lesser extent, for all of the REEs and the slight heavy rare earth fractionation (as measured by Dy/Yb, for example) is a direct result of the extraction of elements from different regions of the melting zone. This result suggests that

Fig. 7. REE patterns calculated for the model shown in Fig. 6. The thin lines show the REE pattern calculated at the surface at different distances from the ridge axis ($x = 0$). The thick grey line shows REE concentrations for the mixture of all of these individual melts. While all the melts that exit the model are in equilibrium with spinel peridotite, differential extraction can still produce a mild 'garnet' signature in the heavy rare earths. The thick line with symbols is the best-fit REE pattern produced by a simplified inversion scheme. All concentrations are normalized to solid source concentrations because melting calculations only give information about changes from source. Specific REE patterns are derived by multiplying these patterns by source concentrations (or source relative to chondrite, etc.).

a 'garnet signature' in stable elements may be less of an indicator of fractional melting and disequilibrium transport (e.g. [47,48]) than it is a measure of the relative geometries and volumes of melt extraction in the garnet and spinel field. [1]

More generally, many of the arguments about the shape and depth of melting, inferred from trace element studies and model inversions (e.g. [11,12]), are actually sensitive to the inherent assumptions about the geometry of melting and melt extraction. Another use of the transport models is as alternative forward models that can be used to explore how various inversion schemes map signals into parameters. As an example, we have used the synthetic REE patterns in Fig. 7 as input to an inversion scheme to find the best-fit 'triangular' melting column model.
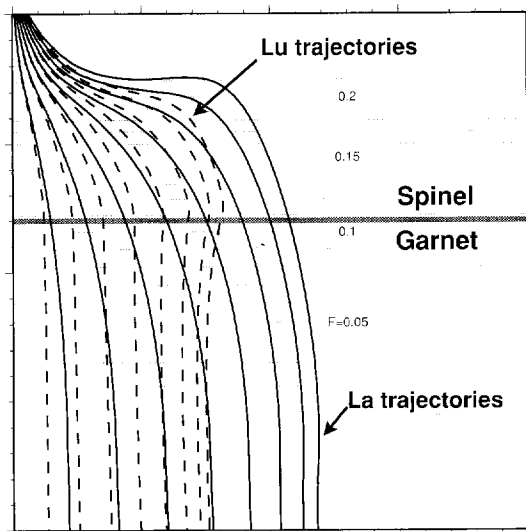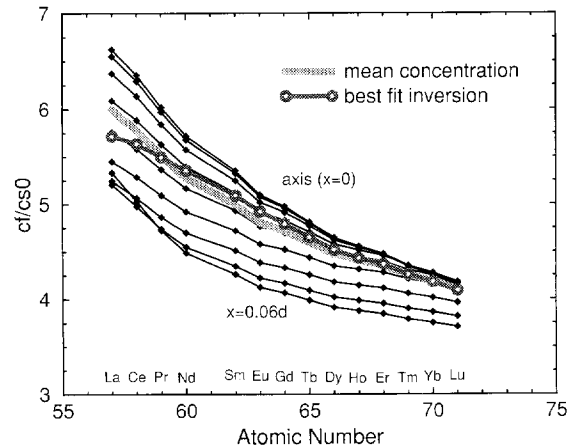

Fig. 6. Trace element trajectories and depletion structure for a more complicated two-layer model used to model REE patterns. This model has the same solid flow field as Fig. 1a but is two times deeper, with a slower melting rate in the deeper region. The total degree of melting is shown by the fine gray contours. This model also has two separate layers with different bulk partition coefficients. These partition coefficients are chosen to be representative of the REE elements in spinel and garnet peridotites (see Table 2). The figure shows trace element trajectories for La and Lu assuming equilibrium transport. There is approximately 10% melting in the garnet field and Lu behaves more compatibly up to this point, reducing the size of the region from which Lu is extracted.

[1] Better arguments for near-fractional melting come from major elements and abyssal peridotites (e.g. [46,49]).

This method is mathematically equivalent to the double integration scheme used by White et al. [12], with some simplifications. The forward model inherent in this scheme assumes fractional melting, complete melt extraction and perfect mixing of all melts from the melting region. The model also assumes that the degree of melting increases linearly with height to a maximum value of F_{max} on-axis. Like the transport model in Fig. 6, this calculation allows for two bulk partition coefficients per element, with the garnet–spinel transition occurring at a constant degree of melting F_1. Because the model used in the inversion has source and partition coefficients identical to the transport model, the only free parameters to be fit are F_{max} and F_1. These are found by minimizing the misfit between the mean concentrations of elements produced by the transport model and by the inversion model (see Appendix A.3). Results are shown in Fig. 7. While the inversion produces an excellent fit, it considerably overestimates the maximum degree of melting and underestimates the amount of melting in the garnet field; that is, the transport model has $F_{max} = 21\%$ with $\sim 11\%$ occurring in the garnet field, while the best-fit inversion needs $F_{max} = 34\%$ with only 5.3% in the garnet field.

The principal reason for the discrepancy between the two model results is that the non-transport model assumes that the composition of the pooled melts includes all of the small-degree melts from the deep, off-axis wings of the melting region. These melts dominate the inversion because they are highly enriched in light rare earths and have the largest garnet signature. Thus, to produce a REE pattern with relatively low La concentration such as Fig. 7, the inversion model must increase the total amount of melting to off-set the enrichment from the wings. However, to also produce a weak garnet signature, the inversion must minimize the amount of melting in the garnet field (although it still requires some garnet melting). The actual reason for the low La values and the weak garnet signature in the transport model, however, is that this model simply does not collect the most distal melts. In this case, melting can begin much deeper and to lesser extents without leaving a strong signal in stable trace elements.

Clearly, further work needs to be done to explore this system in detail and include the additional constraints of U-series nuclides and major elements. The eventual goal is to develop an internally consistent framework for the coupled investigation of both geodynamics and geochemistry in a single system that can provide stronger constraints than either geophysics or geochemistry alone. Such models may give us more insight into the interpretation of available data, and guide the design of more discriminating experiments. Such models need to include melt transport as well as solid flow, however, because this process is the natural link between mantle dynamics and observable geochemistry.

Acknowledgements

Appendix A

A.1. Solution of trace element transport by method of characteristics

A.1.1. Equilibrium transport

To solve Eq. (8) for tracer trajectories and melt concentrations along the trajectory, it is useful to rewrite Eq. (8) as a system of ordinary differential equations using the method of characteristics. If we let the concentration and position of each tracer be a function of the local travel time, τ, such that $c^f(\mathbf{x},t) = c^f(\mathbf{x}(\tau),t(\tau))$ then Eq. (8) can be written:

$$\frac{dc^f}{d\tau} = c^f[\alpha\Gamma + \dot{D}] \tag{19}$$

$$\frac{dt}{d\tau} = 1 \tag{20}$$

$$\frac{d\mathbf{x}}{d\tau} = \mathbf{v}_{eff} \tag{21}$$

Alternatively, it is numerically more stable to define a new variable $U^f = \ln(c^f/c_0^f)$ where c_0^f is the initial melt concentration on the initiation of melting and note that:

$$\frac{dU^f}{d\tau} = \frac{1}{c^f}\frac{dc^f}{d\tau} = \alpha\Gamma + \dot{D} \qquad (22)$$

The system of Eq. (22) and (21) are readily solved using a standard ODE solver (e.g. a 5th order Runge–Kutta Cash–Karp routine [50]) by starting at a point x_0, with initial scaled concentration $U^f = 0$ and integrating forward; $x(\tau)$ is the trace element trajectory, $U^f(\tau)$ records the change in concentration along the trajectory and τ is the transport time along the trajectory.

A.1.2. Disequilibrium transport

In a similar manner, it is possible to decompose Eq. (14) and (15) into a sequential system of ODE's. Starting with Eq. (14) for conservation of composition of the solid residue, we define $U^s = c^s/c_0^s$ and Eq. (14) becomes:

$$\frac{\partial U^s}{\partial t} + \mathbf{V} \cdot \nabla U^s = \left(\frac{1}{D} - 1\right)\frac{\Gamma}{\rho_s(1 - \phi)} \qquad (23)$$

and the RHS is independent of composition. Eq. (23) can then be written as the system of ODE's:

$$\frac{dU^s}{d\tau} = \left(\frac{1}{D} - 1\right)\frac{\Gamma}{\rho_s(1 - \phi)} \qquad (24)$$

$$\frac{dx}{d\tau} = \mathbf{V} \qquad (25)$$

Because the RHS of Eq. (24) is independent of U^s, the integral of this equation depends on the path, but not on the direction that the integral is taken. Thus, to produce a regularly gridded array of concentrations for U^s (e.g., Fig. 2b), start at each gridpoint and shoot backwards to where melting begins. To solve for accumulated melt concentrations, however, requires an explicit forward integration. If we define $U^f = \ln(c^f/c_0^f)$, as before, then Eq. (15) becomes:

$$\frac{\partial U^f}{\partial t} + \mathbf{v} \cdot \nabla U^f = \left(\exp[U^f - U^s] - 1\right)\frac{\Gamma}{\rho_f\phi} \qquad (26)$$

or as a set of ODE's as:

$$\frac{dU^f}{d\tau} = \left(\exp[U^f - U^s] - 1\right)\frac{\Gamma}{\rho_f\phi} \qquad (27)$$

$$\frac{dx}{d\tau} = \mathbf{v} \qquad (28)$$

Eq. (27) is now dependent on the direction in which the integration proceeds. To solve for U^f at a point x_1, first shoot backwards along melt trajectories to find the point where melting begins. Given this x_0 and τ, shoot forward to x_1.

A.1.3. Calculating depletion

The preferred way to calculate the local degree of depletion, F, experienced by any piece of solid in an open system is to calculate the local concentration of a completely compatible element $(D \to \infty)$ using Eq. (23) and note that $F = 1 - c_0^s/c^s = 1 - \exp(-U^s)$. This method is also used by Scott [25]. Note that if $dF_0/dz = F_0^{max}/d$, then $U_{max}^s \sim F_0^{max}$ when $\phi \ll 1$, so that the true F_{max} is less than F_0^{max} when melt extraction is efficient.

A.2. Proof of 2-D effects on axial melts

To understand the effects of passive and active flow for the chemistry of axial melts, consider the behaviour of a completely incompatible element $(D = 0)$ that travels on the characteristic that lies along the axis. For a complete incompatible, the proof is the same for either equilibrium or disequilibrium transport but is easier to demonstrate using the equilibrium equations. For $D = 0$, $\mathbf{v}_{eff} = w(z)$ on-axis and Eq. (21) and (22) can be rearranged into a single ODE in the vertical:

$$\frac{dU^f}{dz} = -\frac{\Gamma}{\rho_f\phi w} \qquad (29)$$

that is, the change in concentration with height up the column depends on the ratio of the local melt production rate and the local melt flux. Now, in 1-D there is a strict relationship between melting rate and flux because 1-D steady-state mass conservation requires that $\partial(\rho_f\phi w)/\partial z = \Gamma$, which can be immediately integrated to show:

$$\rho_f\phi w(z) = \int_0^z \Gamma dz \qquad (30)$$

that is, the melt flux through any point exactly balances the amount of melt produced in the column up to that point. Combining Eq. (30) and (29), it can be shown that the equations for the concentration of a completely incompatible element in a 1-D column become:

$$\frac{c^f}{c_0^s} = \frac{\rho_s W_0}{\int_0^z \Gamma \, dz} \tag{31}$$

that is, the concentration of a completely incompatible element in a 1-D melting column depends on the ratio of the flux of unmelted solid that enters the base of the column to the total amount of melt produced up to a height z (see [20] appendix).

In 2- or 3-D however, conservation of mass requirements occur in the much weaker form $\nabla \cdot [\rho_f \phi w] = \Gamma$, or in integral form for the axis:

$$\rho_f \phi w(z) = \int_0^z \left[\Gamma - \frac{\partial}{\partial x} \rho_f \phi u \right] dz \tag{32}$$

which, for a horizontally convergent melt flux, can be much larger than the flux in Eq. (30).

The difference in concentrations of extremely incompatible elements between passive and active flows actually stems from two different effects. For passive flow, the melting rate on-axis remains similar to the melting rate of a 1-D column, because $\Gamma \alpha W$ and the solid flow field is pretty much constant on-axis. However, the vertical melt flux, $\rho_f \phi w$ increases dramatically with height due to the melt suction effect of Eq. (32). Given the same melting rate but a larger melt flux, the RHS of Eq. (29) is smaller than the 1-D case and, therefore, the change in concentration over the height of the column will be less than the 1-D case. The melts will look like deeper melts and have higher concentrations of incompatible elements.

The strong dilution due to active flow is caused by a different process, but it still arises because mass conservation constraints are much weaker in 2-D. Because of small-scale convection (which is inherently a 2-D effect), both Γ and $\rho_f \phi w$ are larger on-axis; however, the lack of convergence of *melt* flowlines means that the local axial melt flux nearly balances axial production (i.e., Eq. (30) and (31) are approximately valid). Thus, for active flow, the concentration of a completely incompatible element is

still well approximated by Eq. (31). However, because of the convergent *solid* flow within the partially molten region, $\int_0^z \Gamma \, dz$ is much larger on-axis than the passive flow case (see Fig. 1). While $\rho_s W_0$ is also larger, it does not compensate sufficiently for the increase in the total melt production caused by small-scale convection. Thus, a completely incompatible element can show much lower concentrations on-axis than is predicted in the 1-D case.

A similar argument can be made to show that strongly compatible elements are insensitive to either passive or active flow (with equilibrium transport). For a completely compatible element, Eq. (30) and (29), become:

$$\frac{dU^f}{dz} = \frac{\Gamma}{\rho_s(1 - \phi)W} \tag{33}$$

Thus, for adiabatic upwelling where $\Gamma \alpha W$, the change in concentration with height is insensitive to either the melt or solid flow fields. Similar arguments can be made for disequilibrium transport. Unlike equilibrium transport, however, strongly compatible elements are sensitive to the melt flow field and the enhanced axial melt flux tends to enrich the tracers in the melts.

A.3. A simplified inversion scheme

The inversion scheme used in Fig. 7 is the same as used by White et al. [12] with two simplifications: the '1-D' melt distribution is assumed to increase linearly with height and the partition coefficients have only two values. Otherwise, the melt concentrations are integrated twice over the height of the column to produce a 'point and depth average' melt concentration for each element (which is identical to the pooled fractional melts from a 'triangular' melting region). The two free parameters, F_{max} and F_1 are then adjusted to minimize $\chi^2 = \sum_{n=1}^N [(\bar{c}_n^i - \bar{c}_n^i)/\sigma_n]^2$ where $\bar{c}_n^i$ is the mean concentration of element n in the accumulated melts in Fig. 7, $\bar{c}_n^i$ is the mean concentration of the same element predicted by the inversion model and σ_n is a measure of the range in 'natural' variation for each element seen in axial and off-axis melts. The best fit shown in Fig. 7 has $\chi^2 = 0.35$. < /APP >

References

[1] P. Gast, Trace element fractionation and the origin of tholeiitic and alkaline magma types, Geochim. Cosmochim. Acta 32, 1057–1086, 1968.

[2] D.M. Shaw, Trace element fractionation during anatexis, Geochim. Cosmochim. Acta 34, 237–243, 1970.

[3] M.J. O'Hara, Importance of the "shape" of the melting regime during partial melting of the mantle, Nature 314, 58–62, 1985.

[4] T. Plank and C.H. Langmuir, Effects of the melting regime on the composition of the oceanic crust, J. Geophys. Res. 97, 19,749–19,770, 1992.

[5] M.B. Holness and F.M. Richter, Possible effects of spreading rate on MORB isotopic and rare earth composition arising from melting of a heterogeneous source, J. Geol. 97, 247–260, 1989.

[6] D.W. Forsyth, Crustal thickness and the average depth and degree of melting in fractional melting models of passive flow beneath mid-ocean ridges, J. Geophys. Res. 98, 16073–16079, 1993.

[7] Y. Shen and D.W. Forsyth, The initial and final depths of melting beneath mid-ocean ridges, J. Geophys. Res. 100, 2211–2237, 1995.

[8] M.J. O'Hara, Trace element geochemical effects of integrated melt extraction and 'shaped' melting regimes, J. Petrol. 36, 1111–1132, 1995.

[9] C.H. Langmuir, J.F. Bender, A.E. Bence, G.N. Hanson and S.R. Taylor, Petrogenesis of basalts from the famous area; mid-Atlantic ridge, Earth Planet. Sci. Lett. 36, 133–156, 1977.

[10] C.H. Langmuir, E. Klein and T. Plank, Petrological systematics of mid-oceanic ridge basalts: constraints on melt generation beneath ocean ridges, in: Mantle Flow and Melt Generation at Mid-ocean Ridges, J. Phipps Morgan, D.K. Blackman and J.M. Sinton, eds., Am. Geophys. Union Geophys. Monogr. 71, 183–280, 1992.

[11] D. McKenzie and R.K. O'Nions, Partial melt distributions from inversion of rare earth element concentrations, J. Petrol. 32, 1021–1091, 1991.

[12] R.S. White, D. McKenzie and K.R. O'Nions. Oceanic crustal thickness from seismic measurements and rare earth element inversions, J. Geophys. Res. 97, 19,683–19,715, 1992.

[13] D. McKenzie, The generation and compaction of partially molten rock, J. Petrol. 25, 713–765, 1984.

[14] D.R. Scott and D. Stevenson, Magma solitons, Geophys. Res. Lett. 11, 1161–1164, 1984.

[15] D.R. Scott and D. Stevenson, Magma ascent by porous flow, J. Geophys. Res 91, 9283–9296, 1986.

[16] M. Spiegelman, Flow in deformable porous media. Part 1. Simple analysis, J. Fluid Mech. 247, 17–38, 1993.

[17] M. Spiegelman, Flow in deformable porous media. Part 2. Numerical analysis — the relationship between shock waves and solitary waves, J. Fluid Mech. 247, 39–63, 1993.

[18] M. Spiegelman, Physics of melt extraction: Theory, implications and applications, Philos. Trans. R. Soc. London A 342, 23–41, 1993.

[19] N.M. Ribe, The generation and composition of partial melts in the earth's mantle, Earth Planet. Sci. Lett. 73, 361–376, 1985.

[20] M. Spiegelman and T. Elliott, Consequences of melt transport for U-series disequilibrium in young lavas, Earth Planet. Sci. Lett. 118, 1–20, 1993.

[21] F.M. Richter, Simple models of trace element fractionation during melt segregation, Earth Planet. Sci. Lett. 77, 333–344, 1986.

[22] O. Navon and E. Stolper, Geochemical consequences of melt percolation: the upper mantle as a chromatographic column, J. Geol. 95, 285–307, 1987.

[23] N.M. Ribe, Dynamical geochemistry of the Hawaiian plume, Earth Planet. Sci. Lett. 88, 37–46, 1988.

[24] D.J. Stevenson and D.R. Scott, Mechanics of fluid–rock systems, Annu. Rev. Fluid Mech. 23, 305–339, 1991.

[25] D.R. Scott, Small-scale convection and mantle melting beneath mid-ocean ridges, in: Mantle Flow and Melt Generation at Mid-ocean Ridges, J. Phipps Morgan, D.K. Blackman and J.M. Sinton, eds., Am. Geophys. Union Geophys. Monogr. 71, 327–352, 1992.

[26] M. Spiegelman and P. Kenyon, The requirements for chemical disequilibrium during magma migration, Earth Planet. Sci. Lett. 109, 611–620, 1992.

[27] M. Spiegelman and D. McKenzie, Simple 2-D models for melt extraction at mid-ocean ridges and island arcs, Earth Planet. Sci. Lett. 83, 137–152, 1987.

[28] J. Phipps Morgan, Melt migration beneath mid-ocean spreading centers, Geophys. Res. Lett. 14, 1238–1241, 1987.

[29] N.M. Ribe, On the dynamics of mid-ocean ridges, J. Geophys. Res. 93, 429–436, 1988.

[30] M. Rabinowicz, A. Nicolas and J. Vigneresse. A rolling mill effect in the asthenosphere beneath oceanic spreading centers, Earth Planet. Sci. Lett. 67, 97–108, 1984.

[31] D.R. Scott and D.J. Stevenson, A self-consistent model of melting, magma migration and buoyancy-driven circulation beneath mid-ocean ridges, J. Geophys. Res. 94, 2973–2988, 1989.

[32] W.R. Buck and W. Su, Focused mantle upwelling below mid-ocean ridges due to feedback between viscosity and melting, Geophys. Res. Lett. 16, 641–644, 1989.

[33] W. Su and R.W. Buck, Buoyancy effects on mantle flow under mid-ocean ridges, J. Geophys. Res. 98, 12,191–12,205, 1993.

[34] M.J. Cordery and J. Phipps Morgan, Melting and mantle flow beneath a mid-ocean spreading center, Earth Planet. Sci. Lett. 111, 493–516, 1992.

[35] M.J. Cordery and J. Phipps Morgan, Convection and melting at mid-ocean ridges, J. Geophys. Res. 98, 19,477–19,503, 1993.

[36] K. Jha, E.M. Parmentier and J. Phipps Morgan, The role of mantle-depletion and melt-retention buoyancy in spreading-center segmentation, Earth Planet. Sci. Lett. 125, 221–234, 1994.

[37] H. Iwamori, Dynamic disequilibrium melting model with porous flow and diffusion-controlled chemical equilibration, Earth Planet. Sci. Lett. 114, 301–313, 1993.

[38] H. Iwamori, $^{238}U-^{230}Th-^{226}Ra$ and $^{234}U-^{231}Pa$ disequilibria produced by mantle melting with porous and channel flows, Earth Planet. Sci. Lett. 125, 1–16, 1994.

[39] T. Plank, M. Spiegelman, C.H. Langmuir and D.W. Forsyth, The meaning of "mean F": Clarifying the mean extent of melting at ocean ridges, J. Geophys. Res. 100, 15,045–15,441, 1995.

[40] J. Reynolds, Segment scale systematics of mid-ocean ridge magmatism and geochemistry, Ph.D. Thesis, Columbia Univ./LDEO, 1995.

[41] A.W. Hofmann, Chemical differentiation of the earth: Relationship between mantle, continental crust and oceanic crust, Earth Planet. Sci. Lett. 90, 297–314, 1988.

[42] S.S. Sun and W.F. McDonough, Chemical and isotopic systematics of oceanic basalts; implications for mantle composition and processes, in: Magmatism in the Ocean Basins, A.D. Saunders and M.J. Norry, eds., Geol. Soc. London Spec. Publ. 42, 313–345, 1989.

[43] W.F. McDonough and F.A. Frey, REE in upper mantle rocks, in: Geochemistry and Mineralogy of Rare Earth Elements, B. Lipin and G.R. McKay, eds., pp. 99–145, Mineral. Soc. Am., 1989.

[44] M.M. Hirschmann, E.M. Stolper and M.S. Ghiorso, Perspectives on shallow mantle melting from thermodynamic calculations, Mineral. Mag. 58a, 418–419, 1994.

[45] P. Asimow, M. Hirschmann, M. Ghiorso, M.J. O'Hara and E. Stolper, The effect of pressure induced solid–solid phase transitions on decompression melting of the mantle, Geochim. Cosmochim. Acta, in press.

[46] R.J. Kinzler, Melting of mantle peridotite at pressures approaching the spinel to garnet transition: application to the generation of mid-ocean ridge basalts, J. Geophys. Res., submitted.

[47] B. Salters and S. Hart, The hafnium paradox and the role of garnet in the source of mid-ocean ridge basalts, Nature 342, 420–422, 1989.

[48] S.R. Hart, Equilibration during mantle melting: A fractal tree model, Proc. Natl. Acad. Sci. USA 90, 11,914–11,918, 1993.

[49] K.T.M. Johnson and H.J.B. Dick, Open system melting and temporal and spatial variation of peridotite and basalt at the Atlantis II fracture zone, J. Geophys. Res. 97, 9219–9241, 1992.

[50] W.H. Press, B.P. Flannery, S.A. Teukolsky and W.T. Vetterling, Numerical Recipes, Cambridge Univ. Press, Cambridge, 2nd ed., 1992.